Static and dynamic indentation response of basal and prism plane sapphire

Edward J. Haney [1], Ghatu Subhash [*,1]

Mechanical and Aerospace Engineering, University of Florida, Gainesville, FL 32611, USA

Received 17 September 2010; received in revised form 23 February 2011; accepted 2 March 2011
Available online 31 March 2011

Abstract

Static and dynamic indentation experiments are conducted on sapphire along the $c[0\,0\,0\,1]$ and $a[1\,1\,\bar{2}\,0]$ crystallographic axes to determine the loading rate dependence on its mechanical response. Static hardness is measured using a conventional Vickers tester while the dynamic hardness is measured using a custom test fixture based on split Hopkinson pressure bar technique with the capability to produce single indentations at strain rates of roughly $10^3\,\text{s}^{-1}$. Static and dynamic hardness values as well as characteristic fracture response for both axes are compared at a range of indentation loads. The results indicate that dynamic hardness increases by 10% and 12% over static hardness for basal and prism plane sapphire, respectively. Observed crack orientations due to indentation of the *a*- and *c*-planes are consistent with the expected location of twinning or slip on the $r(0\,1\,\bar{1}\,2)$, $(1\,\bar{1}\,0\,2)$, $(\bar{1}\,0\,1\,2)$ and $c(0\,0\,0\,1)$ planes for both static and dynamic indentations. Prism slip is also suspected to interact with rhombohedral twinning systems to create a weakened zone oriented along the *c*-axis. Static indentations yielded well defined crystallographically oriented cracks with repeated directional switchbacks indicating a zone of competition between the two crack systems. Dynamic indentations, on the other hand, resulted in shorter and less jagged cracks accompanied by increased localized spalling beneath each indentation site as compared to the static indentations. This mode of fracture would suggest a shift in energy dissipation mechanism from crystal axis oriented long crack propagation under static loading to micro cracking that is independent of crystallographic orientation under higher strain rate events.
© 2011 Elsevier Ltd. All rights reserved.

Keywords: C. Fracture; C. Hardness; C. Mechanical properties; Transparent armor; Sapphire

1. Introduction

Sapphire, a single crystal form of pure aluminum oxide (Al_2O_3), is a leading candidate material for many extreme environment optical applications including protective shields, ground and air vehicle windows, optical lenses exposed to harsh environments and transparent armor[1–3] due to its excellent mechanical properties, optical transparency, IR transmission and commercial availability. Common industrial techniques used to grow sapphire crystals include Vernouilli, Czochralski, Kyropoulos, gradient solidification method (GSM), heat-exchanger method (HEM) and edge defined film fed growth (EFG). Each method is able to produce crystals of different orientations, sizes and qualities. A comprehensive review of the history of sapphire crystal growth and a comparison of methods is presented by Harris.[4]

Sapphire, however, has a hexagonal–scalenohedral crystal structure resulting in anisotropic material behavior that is highly dependent on crystal orientation. Sapphire is most commonly manufactured in $c(0\,0\,0\,1)$, $m(1\,0\,\bar{1}\,0)$, $a(1\,1\,\bar{2}\,0)$ and $r(1\,\bar{1}\,0\,2)$ surface orientations. Mechanical, thermal, electrical and optical properties are widely reported to vary depending on axis orientation. For example, hardness, Young's modulus, shear modulus and thermal conductivity are highest perpendicular to the *c*-axis, while tensile strength, flexural strength and dielectric constant are highest parallel to the *c*-axis.[5,6] It is also interesting to note that a significant loss in compressive strength occurs at elevated temperatures, most notably when the compressive stress is parallel to the *c*-axis.[7] This is found to be a result of reduced resolved shear stress required to activate rhombohedral twinning.[8] In addition, optical birefringence or double refraction occurs along all axes except for the *c*-axis.[6] Therefore, the *c*-axis is optically unique and is often referred to as the optical axis.[6,9]

An important application of sapphire is as a strike face material in transparent armor. Since the pioneering work of Wilkins et al.,[10–15] it has been known that dynamic material characterization and an understanding of the relationships

between competing mechanisms are paramount for ceramic armor design. The notion that hardness and fracture toughness are the most relevant material parameters that limit the ballistic strength of ceramics was first proposed by Woodward,[16] who noticed that hardness was important to blunt a projectile but fracture reduced the ballistic strength of ceramics. LaSalvia[17] later presented the notion that hardness can estimate the performance potential of a ceramic while fracture toughness is a limiting measure that determines the ability to meet that potential.

More recently, Krell and Straßburger[18] presented a hierarchy of key influences governing ballistic strength of transparent ceramics. They postulated that the initial phase during ballistic impact, termed dwell phase[19,20] was governed by dynamic stiffness and that the latter phase or penetration phase,[21] is governed by the inertial impedance which is based on the mode of fragmentation and hardness. In this study it was suggested that hardness should be replaced by a dynamic measure (e.g. Hugoniot elastic limit) although due to a linear correlation present between static hardness and HEL measurements, the more easily measurable static hardness was employed.

Kanel et al.[22,23] conducted extensive research on shock loading of sapphire along several crystal axes to determine the Hugoniot elastic limit (HEL), defined as the dynamic compressive strength under uniaxial strain loading, using flyer plate experiments. While this testing reveals the rate dependant behavior of sapphire strength, it does not provide insight into the strain rate effect on hardness and the mode of indentation fracture under dynamic loads. Dynamic indentation experiments[24–27] on the other hand can provide such information. Variants of these experiments have been successfully employed to provide insight into the strain rate dependence of several crystalline materials.[28–32] In this manuscript we will provide a comparative analysis of hardness as well as fracture initiation and propagation characteristics of *a*- and *c*-plane sapphire under static and dynamic indentations.

Table 1
Mechanical properties of sapphire at 25 °C.[6]

	Parallel to *c*-axis	Perpendicular to *c*-axis
Density (g/cm^3)		3.97
Young's modulus (GPa)	435	386
Shear modulus (GPa)	175	145
Poisson's ratio		0.25–0.30 (orientation dependant)
Biaxial flexural strength (MPa)	1035	760
Compressive strength (GPa)	1.97	2
Tensile strength (GPa)	0.432	0.302
Vickers hardness (GPa)—10 N	17.4	15.6
K_{IC} (MPa m$^{1/2}$)[1]	4.5	2.43

2. Experimental procedure

Square tiles of dimensions 76 mm × 76 mm × 7.6 mm of *a*-plane sapphire were obtained from Saint Gobain Crystals, Milford, NH. These tiles were grown using the edge defined film-fed growth (EFG) process.[33] Table 1 provides basic material properties.[6] Fig. 1 is an illustration of the sample tiles indicating the dimensions and crystallographic orientation.[5] Several 6 mm cube samples were then cut from the tile exposing both *a* and *c* surfaces. Both *a* and *c* surface samples were then ground and polished to remove all visually distracting surface scratches created by the manufacturing or cutting process using progressively finer silicon carbide grinding media (320, 400, 600, 800 and 1200 grit) followed by diamond paste polishing medium (6, 1 and 0.5 μm). The quality of the resulting polished surface was evaluated visually under an optical microscope at 100× magnification. Several static indentations were made on both the *a*- and *c*-planes of the test samples using a Vickers indenter (Wilson® Instruments Tukon® 2100B) with indentation loads in the range of 0.5–19.6 N (0.05–2 kg).

Dynamic indentation testing was conducted using a dynamic indentation hardness tester (DIHT).[24–27] A schematic and picture of the test apparatus is shown in Fig. 2. This testing
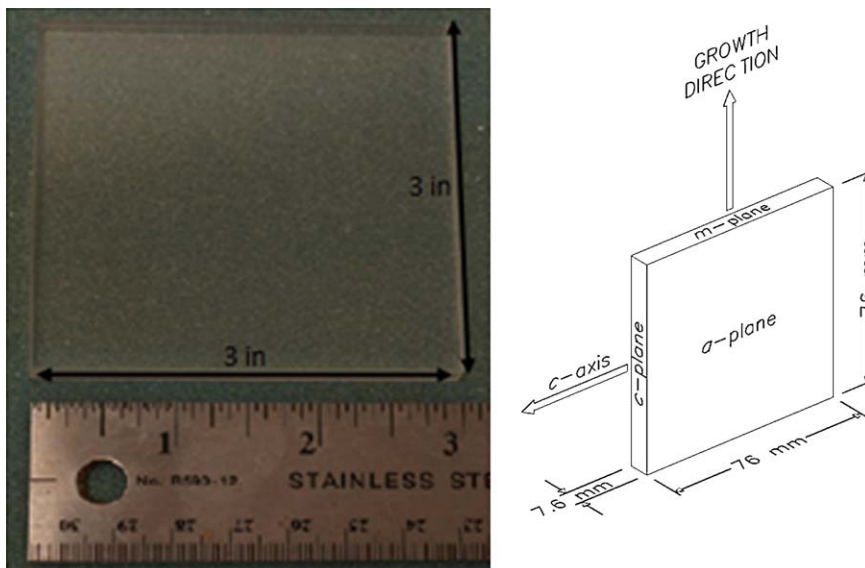

Fig. 1. Schematic of the orientation of *a*-plane sapphire crystal tile supplied by Saint-Gobain crystals.
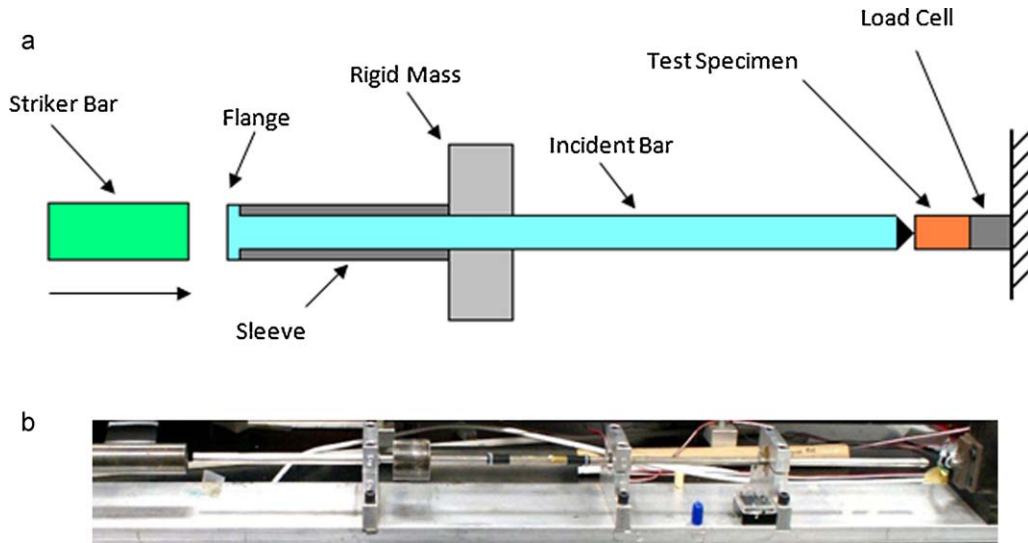
Fig. 2. Schematic of dynamic indentation hardness tester.

technique is based on a modified split Hopkinson pressure bar (SHPB) setup which is able to generate a single Vickers indentation with a loading duration of approximately 50–200 μs.[34] This is accomplished by acceleration of a striker bar by a pneumatic pressure gun towards a flanged incident bar. The incident bar has a Vickers indenter press fit to one end and a momentum trap on the impact end. The test specimen was positioned between the Vickers indenter and a load cell which is anchored to a rigid support. No gap was allowed between the Vickers tip and the specimen test surface. The striker bar impact onto the incident bar creates an elastic compressive pulse followed by a tensile wave (from the momentum trap) both of which travel the length of the incident bar towards the indenter end. The compressive pulse causes a single indentation on the test sample and the tensile pulse retracts the Vickers tip away from the test specimen. Both of these pulses reverse in sign and travel back towards the impact end where the reflected tensile pulse is captured by the momentum trap and the reflected compressive wave reflects back again as a tensile wave traveling towards the indenter tip. This wave travels back and forth in the bar as a tensile wave towards the indenter tip and as a compressive wave traveling towards the impact end. Thus, all of the tensile waves traveling towards the indenter cause the indenter tip to retract away from the specimen.[24,34] The time-based indentation load signal is captured using a high frequency load cell and a digital oscilloscope. Unlike the static indentation, the load of the dynamic indenter cannot be precisely set due to the slight variations in the velocity of the striker bar as it travels through the gas gun (i.e. frictional effects). Therefore, a minimum of 50 indentations was conducted at room temperature on each test specimen to insure a varied load range. Hardness values were calculated based on the measured indentation diagonal lengths and the measured load. Crack lengths and crack orientations were measured for both static and dynamic indentations using an optical microscope. The measurements were then compared to assess the strain rate effect on hardness and crack lengths for both orientations of sapphire.

It should be noted that the convention used to measure and annotate crack lengths differs slightly for sapphire due to the nature of crystallographically aligned crack systems. Traditionally, radial crack length "2c" is defined as the distance between the two opposing crack tips originating from the opposing Vickers indentation corners.[35] In the case of indentation on sapphire, corner cracks do not appear, instead cracks initiate preferentially along specific crystallographic planes irrespective of indentation corner location. Therefore, for the purposes of this study the crack length "2c" is simply defined as the distance between two opposing crack tips oriented along the same crystallographic plane. These cracks may or may not emanate from the corners of the indentation but will always propagate along predetermined crystallographically oriented directions.

3. Results and discussion

3.1. Static and dynamic indentation hardness

The static and dynamic hardness values for *a*- and *c*-plane sapphire as a function of indentation load are provided in Fig. 3. The static hardness values are reported as the average of at least 10 indentations at each load while the dynamic hardness values are shown as individual data points. The data for both surfaces was curve fit in Fig. 3(c) as per Meyer's law[36]:

$$P = Ad^n,$$

where P is the indentation load, d is the indentation diagonal, A is the Meyer's prefactor and n is the Meyer exponent. Both sapphire orientations demonstrated a noticeable indentation size effect (ISE) with the *c*-plane being more pronounced than the *a*-plane. When the data is plotted in the Meyer's law format this difference in ISE between the planes can be numerically established. The Meyer exponent, a measure of the ISE, was found to range from 1.81 for *a*-plane configurations to 1.84 for *c*-plane configurations. These values were consistent with previous ISE studies of single crystal oxides.[37,38]
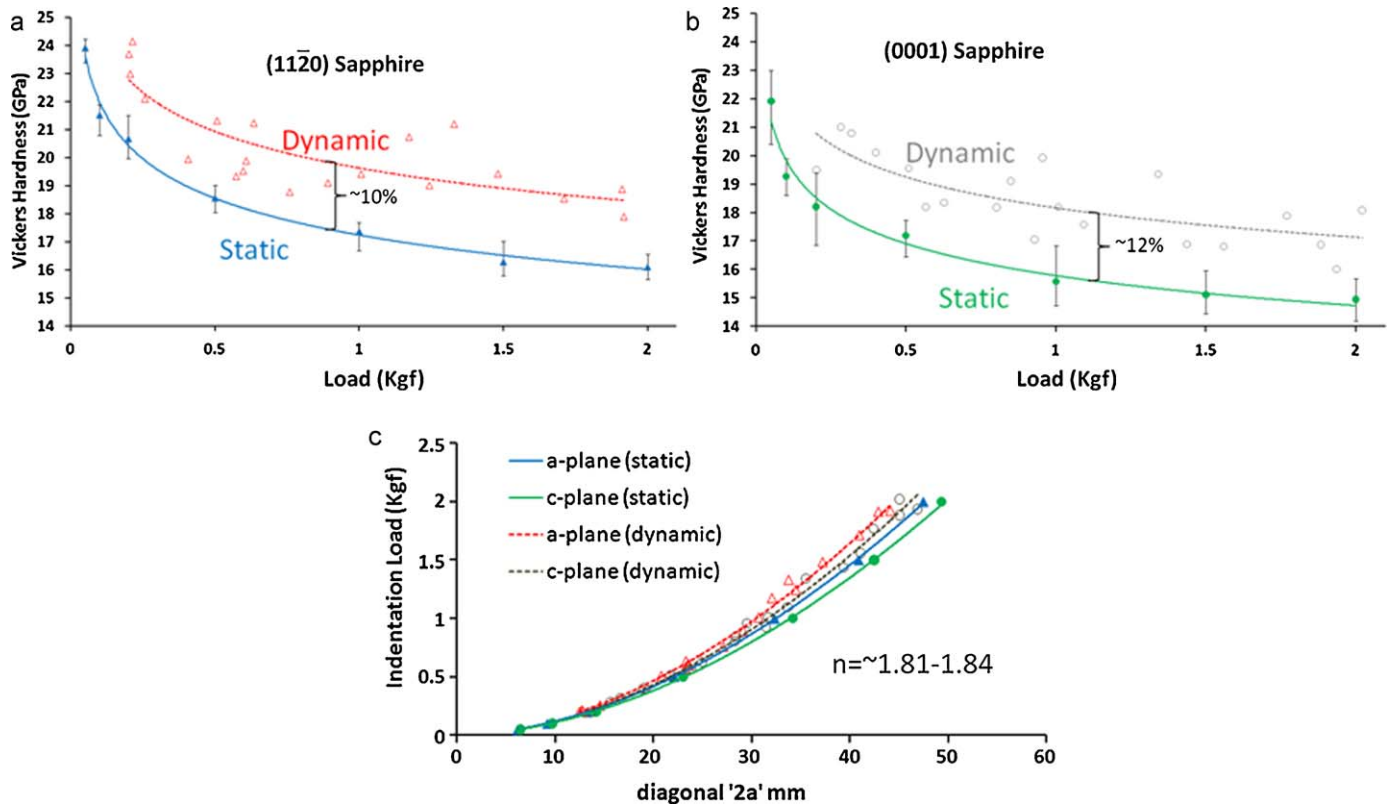
Fig. 3. Static and dynamic hardness trends as a function of indentation load for (a) (1 1 2 0) sapphire, (b) (0 0 0 1) sapphire and (c) Meyer's law fit for the above data.

Both *a*- and *c*-plane sapphire demonstrated an increase in hardness under dynamic indentation. The *c*-plane sapphire yielded a slightly higher increase (12% versus a 10%) than for *a*-plane sapphire. These results are similar to earlier reports of dynamic indentation on polycrystalline alumina.[28] These results are also consistent with Tymiak et al.[32] who reported an increase in yield point of *a*- and *c*-plane orientations with increased loading rates. It is also interesting to compare the greater strain rate sensitivity of the *c*-plane sapphire to the findings of Kanel,[22,23] who reported the largest increase (51%) in the HEL response with increased impact velocity for sapphire along the *c*-axis as compared to only 47% along the *m*-axis. The results demonstrate a correlation of the rate sensitivity of hardness with published HEL values and could be considered when utilizing sapphire for ballistic applications.

The measured indentation hardness did not seem to be dependent on the orientation of the Vickers indenter tip with respect to sapphire crystal orientation. This result was inconsistent with earlier findings of anisotropy in Knoop hardness on sapphire basal plane.[39] It is, however, acknowledged that anisotropy exists on sapphire basal plane. The discrepancy is believed to be due to the fact that Vickers hardness is calculated based on an average of two equal length indenter diagonals while Knoop hardness is calculated purely by the length of the long diagonal. It is, therefore, expected that the anisotropic response is averaged out during Vickers hardness calculations while it is captured during Knoop calculations.

3.2. Fracture behavior

As mentioned earlier, the symbiotic relationship between hardness and fracture behavior is of importance to fully understand the behavior of ceramics under dynamic events such as ballistic impact. In the case of sapphire, indentation creates surface features and fracture patterns that are unique in appearance due to its preferential crystallographic fracture planes, see Fig. 4. The origin, the evolution and the strain rate sensitivity of these surface feature patterns have been studied extensively over the past 6 decades. The appearance of these unique fracture patterns surrounding an indentation impression in sapphire was first reported by Attinger[40] who described the appearance of oriented fissure-like cracks. Hockey[41] first identified the existence of basal and rhombohedral micro-twins surrounding the indentation impressions on single crystal sapphire but was reluctant to fully attribute twinning mechanisms as the source of crack formations. Several subsequent indentation studies[42–45] performed on various sapphire orientations reported observations of basal and rhombohedral twinning as well as basal, rhombohedral, prism and pyramidal slip. Nowak et al.[46] first developed an effective resolved shear stress (ERSS) model that estimated the peak shear stress acting on slip and twinning systems and consequently proposed a "T-parameter" which predicted the activation of each slip and twinning systems during indentation of *a*-$(1\bar{2}10)$, *m*-$(10\bar{1}0)$ and *c*-(1000) planes of sapphire. For example the peak probability for rhombohedral twinning on the *c*-plane was predicted at relative angles of 0°, 120° and 240° with no experimental correlation presented. The
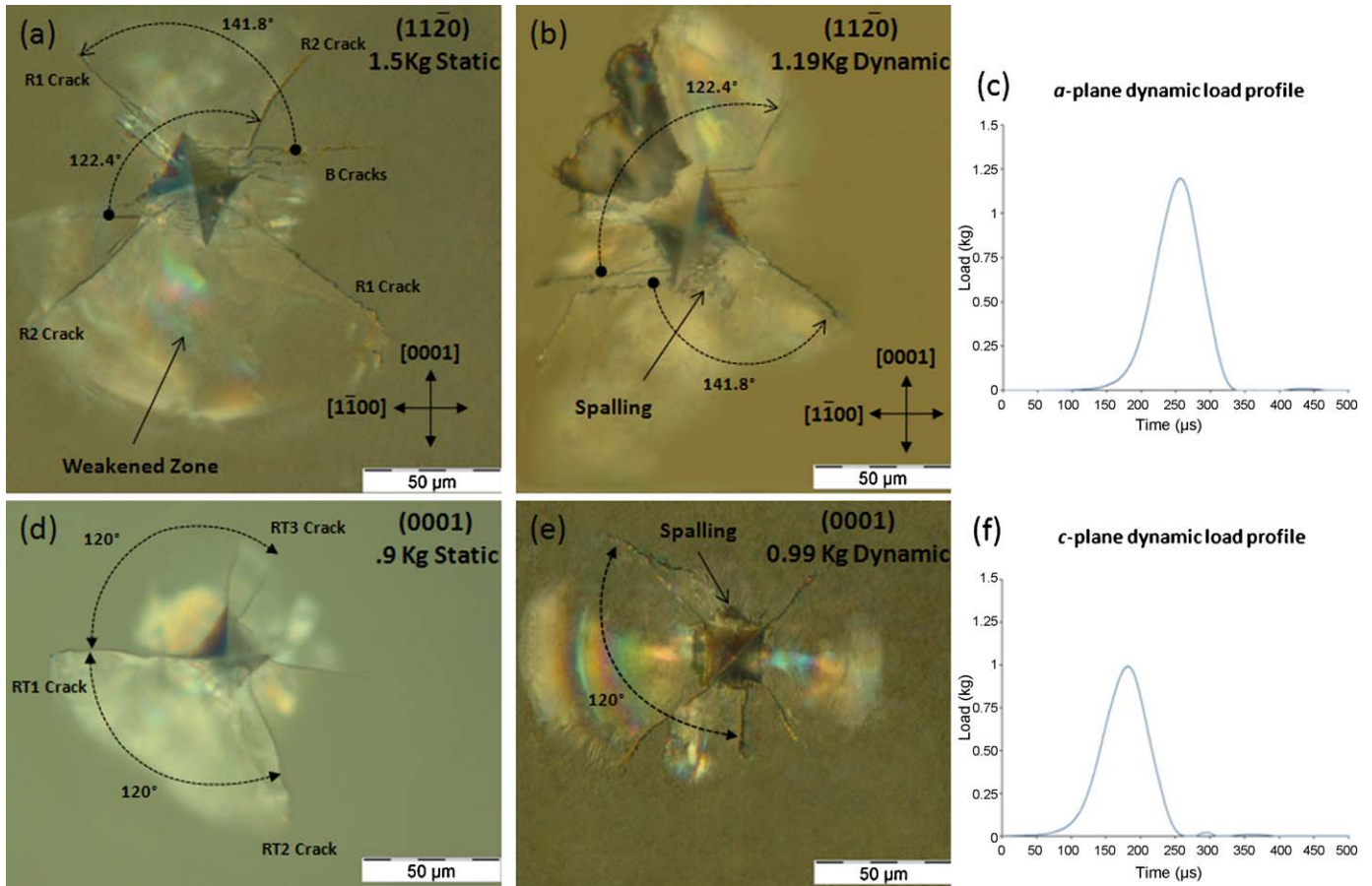
Fig. 4. Fracture patterns due to (a) static and (b) dynamic indentations and (c) the associated dynamic indentation load profile *a*-plane and (d–f) on *c*-plane sapphire.

peak probability of basal twinning on the *a*-plane was predicted to occur at relative angles of 90° and 270° (axisymmetric with respect to the [0 0 0 1] direction) while the peak probability of rhombohedral twinning on the *a*-plane to be at relative angles of 90°, 225° and 315°. Comparisons of predictions of slip and twinning system activation probability were found to poorly correlate to the experimental observations of cracks and linear surface features on *m*-plane sapphire.[47,48] In fact their experimental observations indicated basal twinning rather than rhombohedral twinning to occur at 90°, 225° and 315°. Additionally, Nowak et al.[46] described the appearance of surface traces on both *a*- and *m*-prism planes to be essentially the same with only a trivial 90° shift in angular positions. Subsequent experimental findings has demonstrated that the patterns of plastic deformation are distinctly different between *a*- and *m*-plane sapphire.[32,49] These findings were later reinforced by Tymiak and Gerberich[50] and Tymiak et al.[51] through analytical RSS modeling and FEA analysis. While the modeling efforts of Nowak et al.[46] did not precisely capture all of the observed trends, their pioneering work provided a first look at surface orientation effects on patterns of contact-induced plasticity in sapphire. Additionally, the significance of the role of basal and rhombohedral twinning on contact induced plasticity in sapphire was predicted.

More recent experimental findings from Kim and Kim[49] attempted to correlate experimentally observed surface traces to the intersection of sapphire crystal planes. Based on observa-

tions of fracture sequence of (1 1 $\bar{2}$ 0) sapphire with a physical vapor deposited TiN coating they reported a relative angle of 122.4° between what they asserted as rhombohedral and basal twinning traces, see Fig. 5. This angle corresponded with the
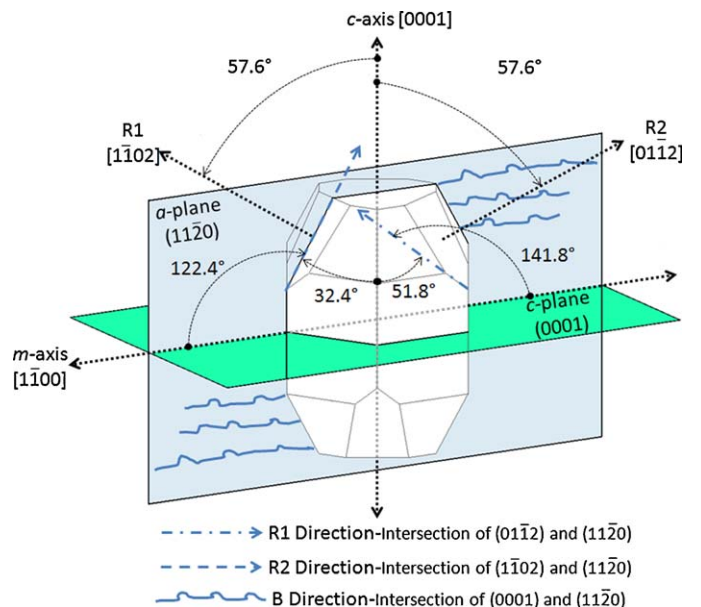

Fig. 5. Schematic of crystal axes projected angles and the relevant preferential crack systems.

crystallographic intersection of the *r*-plane ($1\bar{1}02$) with the *a*-plane ($11\bar{2}0$) yet did not provide a rationale for the appearance of this twinning trace over other possible rhombohedral twinning systems. Most recently, Haney and Subhash[52] provided a comprehensive description of basal and rhombohedral crack plane interactions due to sequential Vickers indentations on *a*-plane sapphire.

Modeling efforts by Tymiak and Gerberich[50] yielded a resolved shear stress (RSS) distribution map for all of the known slip and twinning systems. The model produced an upper and lower bounds for the critical resolved shear stress (CRSS) required to activate a given deformation system at room temperature due to indentation. Their modeling provided a good correlation with previous experimental observations. In particular, the earlier findings of Kim and Kim[49] was rationalized due to indications of a higher RSS for the observed rhombohedral twinning system over other possible rhombohedral twinning systems. Although the results of Tymiak and Gerberich[50] correlated well with the observations of Kim and Kim[49] they expressed a reluctance to attribute the surface features to twinnings without TEM analysis to confirm.

Static and dynamic indentations on basal (*c*-plane) and prism (*a*-plane) plane sapphire, shown in Fig. 4, reveal three distinct surface features. Static indentations on *a*-plane ($11\bar{2}0$) sapphire at loads as low as 1 N (0.1 kg) produced a series of wavy traces oriented perpendicular to the *c*-axis [0001] (images not shown here for brievity). The orientations of these traces are consistent with earlier findings from Chan and Lawn,[43] Nowak and Sakai[46] as well as Kim and Kim[49] who all identified these features as basal twins. With increased load evidence of some crack nucleation along these traces becomes evident although not all traces result in fracture formation, see Fig. 4(a) and (b). Consequently features identified as cracks following this orientation are depicted in all subsequent figures as B-cracks. At 2 N (0.2 kg) loads, a second set of cracks oriented at approximately 51.8° relative to the *c*-axis or 141.8° relative to the B-crack orientation appeared. This crack orientation is consistent with the intersection of the ($01\bar{1}2$) *r*- and ($11\bar{2}0$) *a*-planes and is referred to as R1-crack. With further increase in load a third crack system (referred to as R2-crack) oriented at approximately 38.2° relative to the *c*-axis or 122.4° relative to the B-cracks also appeared. This orientation is consistent with the intersection of the ($1\bar{1}02$) *r*- and ($11\bar{2}0$) *a*-planes. In order to better describe the idea of axis projection, a three-dimensional schematic illustrating the projection of basal and rhombohedral twinning cracks onto the *a*-plane is shown in Fig. 5. The measured surface orientation of the B-cracks and the R2-cracks (122.4° relative to B-cracks) were consistent with the prediction of surface traces of well defined twins presented by Tymiak and Gerberich[50] as well as Kim and Kim[49] but the R1 feature (141.8° relative to the B feature) was not presented by either studies although Tymiak and Gerberich did mention that if other rhombohedral twinning systems were activated they would appear at 141.8° relative to the B features. Although TEM analysis would be needed to provide unambiguous conclusions as to the origin of the observed features, the measured angles of each feature suggest basal and rhombohedral twinning or slip as the source of fracture. It is

also noted from the crack orientations that these cracks do not necessarily initiate from the corners of the Vickers indentation. This would indicate that the energy required to propagate cracks along these preferential directions is lower than what is required to produce radial cracks even with stress concentrations at the indenter corners.

Upon closer inspection the B-cracks tended to have a jagged appearance shown in the enlarged views of the micrographs as seen in Fig. 6. The crack front seems to repeatedly switch between B-crack and R2-crack directions in a periodic manner. Eventually, the R2 direction dominates and a permanent change in direction is witnessed. This behavior indicates a competition between B and the R2 systems possibly due to a combined effect of the critical stress differences between crystallographic planes and the applied stress field.

It is also interesting to note that both the R1 and R2 rhombohedral cracks would bridge between the zones along the *c*-axis [0001] direction while they would not bridge in zones oriented along the *m*-axis. These zones are identified as "weakened zones" in Figs. 4a and 6. This tendency to bridge is believed to be encouraged by prism slip mechanisms which have the highest shear stress concentrations in the area oriented along the *m*-axes per Tymiak and Gerberich's model.[50] With increasing macroindentation load, this region tends to laterally crack in a more severe manner than other regions surrounding the indentation site. This phenomenon creates an inherently weak zone surrounding the indentation site. In our future work, we will demonstrate the importance of the presence of this weakened zone during multiple interacting vickers indentation and relate these crack systems to multi-hit performance of a sapphire target.

Indentations on *c*-plane sapphire produced cracks propogating at angles of 120° relative to each other with additional "corner cracks" propagating from the corners of the indenter. These crack orientations seem to be consistent with the angular separation of peak probability for activation of rhombohedral twinning on basal plane sapphire as proposed by Nowak et al.[43–46] Again without TEM analysis it is presumptuous to state the exact origins of these cracks.

For both surface orientations, cracks due to dynamic indentation appear in a similar orientation as the those due to static indentation but are generally shorter and are accompanied with an increase in localized spalling underneath the indention, see Fig. 7. The half crack length as a function of indenter diagonal is shown in Fig. 8. The crack length measurements indicate a reduced crack length as a function of indent size for both orientations under dynamic loading as compared to static loading, yet had similar slopes. A 20–30% reduction in long crack length can be noted under dynamic loads when comparing to static indentations at similar loads. This again reinforces the idea that the behavior of sapphire tends to shift from long crack propagation to localized micro-cracking during high strain rate indentations.

It is also interesting to note that while the B-cracks seemed to initiate at a lower load (see Fig. 8b), R1 cracks had a higher rate of growth under increasing loads than the basal cracks (Fig. 8a). Although this difference is minor it again illustrates the idea of a crossover of preferential crack systems from basal to rhombohedral under increasing loads.
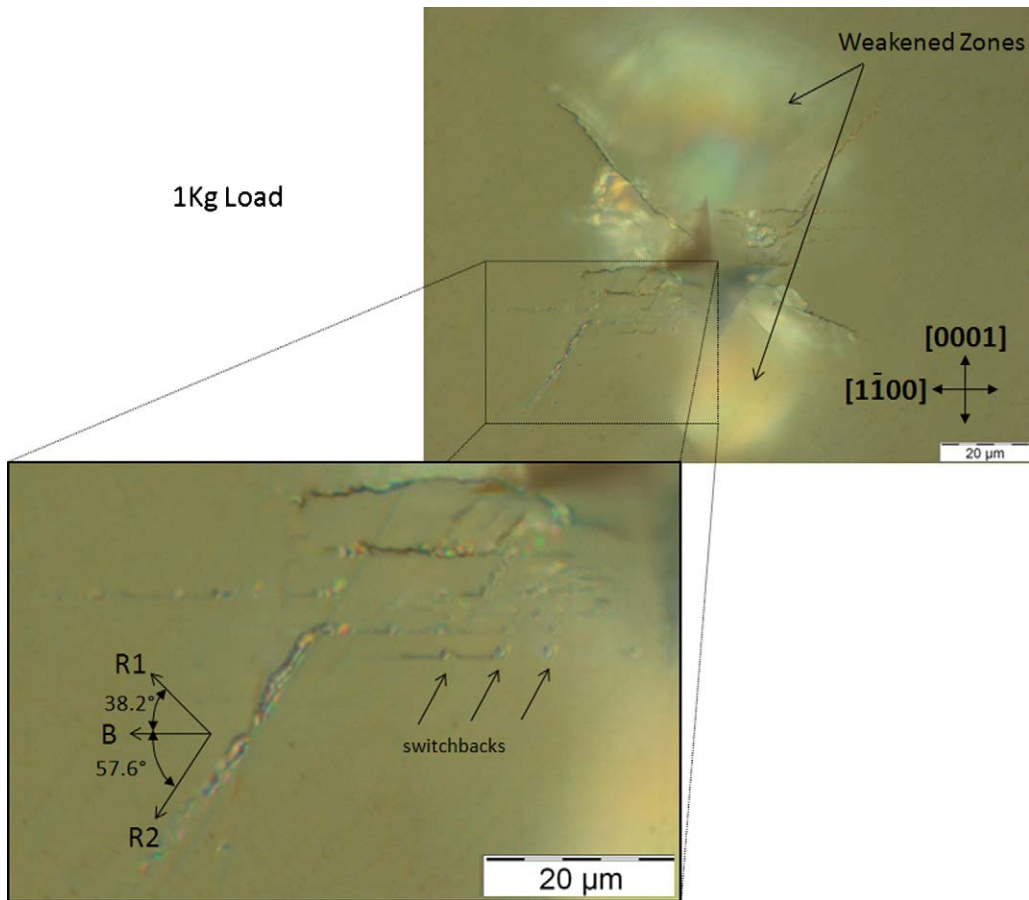
Fig. 6. Enlarged view of jagged appearance of B cracks during static indentation.
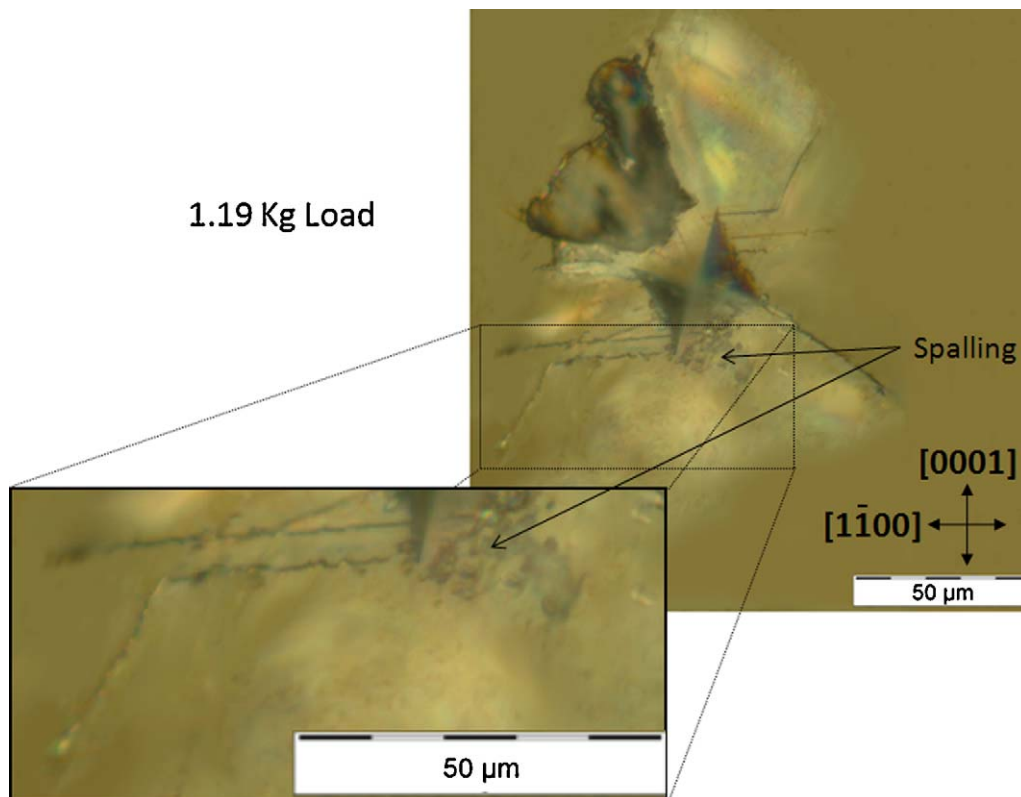

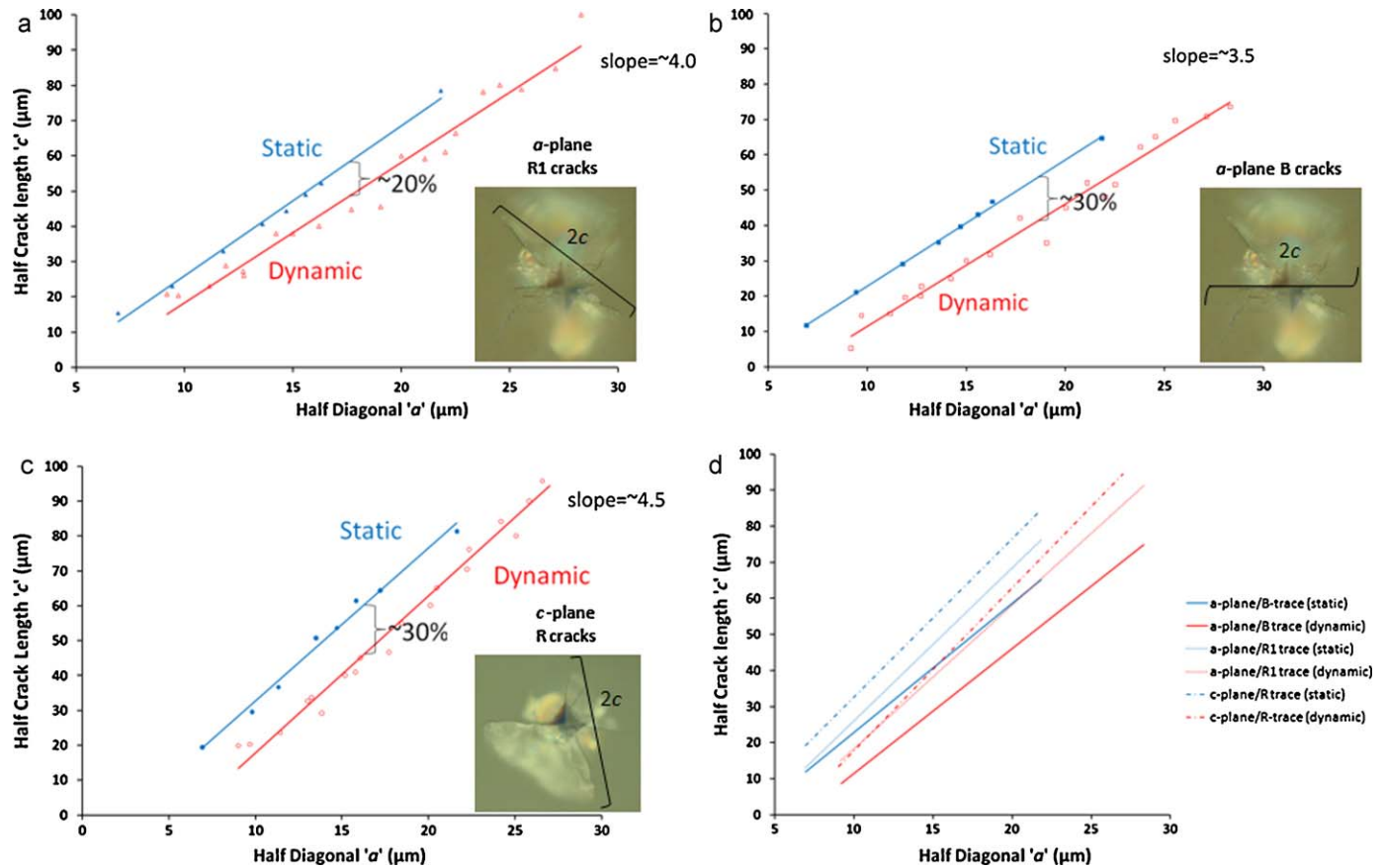Fig. 7. Increased spalling during dynamic indentation.

Fig. 8. Half-crack length 'c' as a function of half diagonal length 'a' under static and dynamic indentations for (a) R1-cracks on a-plane sapphire, (b) B-cracks on a-plane sapphire, (c) R1-cracks on c-plane sapphire and (d) trend lines for all the data combined.

The hardness and crack length results provided in this manuscript may have some relevance to sapphire behavior under projectile impact. It appears that projectile defeat is more likely with a-plane configuration rather than c-plane due to the combination of superior hardness and a reduced crack propagation behavior. In addition, although hardness increases under dynamic conditions for both orientations, the crack length reductions were accompanied with increased spalling and material comminution. This shift in fracture behavior demonstrates the idea that under dynamic conditions, energy is dissipated in a smaller region surrounding the indentation site with a greater reduction in local material structural adhesion but with a higher overall structural integrity as cracks are less prone to propagate large distances. This behavior could provide insight into the mechanisms that control the transition from interface defeat to penetration in sapphire materials as impact velocity increases.

4. Conclusions

Both basal and prism plane sapphire exhibited increased hardness under dynamic indentation and a noticeable indentation size effect. Basal plane sapphire was slightly more sensitive to ISE with a Meyer's exponent of 1.85 versus 1.81 for prism plane. Basal plane sapphire was also more sensitive to strain rate hardening effects with a 12% increase in hardness over static versus a 10% increase for prism plane sapphire. The resultant surface pat-

terns correlate well with previous experimental and analytical studies reported elsewhere. Wavy features (B) oriented along the basal plane are likely due to basal twinning and initiated at lower loads than other cracks oriented along the rhombohedral planes. The cracks (R1 and R2) that are oriented along the rhombohedral planes are possibly due to rhombohedral twinning or slip and with increased loads emerge as the preferential fracture modes. It was observed that cracks propagating along the basal plane would alternate between B and R2 crack directions demonstrating a competing mode of crack propagation and differing reactions to applied stress fields. Weakened zones surrounding a-plane indentation sites are located along the c-axis. Crack behavior seemed to shift from long crack propagation to micro cracking and spalling under dynamic indentations. A 20–30% reduction in crack length was noted under dynamic conditions. Finally, the fracture mode observed under dynamic indentation has been related to the behavior of sapphire under impact conditions.

References

1. Patel PJ, Gilde GA, Dehmer PG, McCauley JW. Transparent armor. *AMPTIAC Q* 2000;**4**(3):1–17.
2. Normandia MJ, Lasalvia JC, Gooch WA, McCauley JW, Rajendran AM. Protecting the future force: ceramics research leads to improved armor performance. *AMPTIAC Q* 2004;**8**(4):21–7.
3. Patel PJ, Gilde GA. Transparent armor materials: needs and requirements. In: McCauley JW, Crowson A, Gooch Jr WA, Rajendran AM, Bless SJ, Logan KV, Normandia M, Wax S, editors. *Ceramic armor materials by design, vol. 134. Ceramic transactions*. Hoboken, NJ: Wiley; 2002. p. 573–86.
4. Harris DC. A century of sapphire crystal growth: origin of the EFG method. In: *Proc SPIE 7425, 742525*. 2009. p. 12.
5. *Saint Gobain crystals product literature*. http://www.photonic.saint-gobain.com/uploadedFiles/SGphotonic/Documents/sapphire-material-products-properties.pdf [Last Accessed 1-12-11].
6. Dobrovinskaya ER, Lytvynov LA, Piskchik V. *Sapphire: material, manufacturing, applications*. New York: Springer; 2009.
7. Schmid F, Harris DC. Effects of crystal orientation and temperature on the strength of sapphire. *J Am Ceram Soc* 1998;**81**(4):885–93.
8. Scott WD, Orr KK. Rhombohedral twinning in sapphire. *J Am Ceram Soc* 1983;**66**(1):27–32.
9. Vetrov VN, Ignatenkov BA. Birefringence in synthetic sapphire lenses. *J Opt Technol* 2006;**73**(5):349–51.
10. Wilkins M, Honodel C, Sawle D. *An approach to the study of light armor*. Lawrence Radiation Laboratory Report # UCRL-50284; 1967.
11. Wilkins M, et al. *Second progress report of the light armor program*. Lawrence Radiation Laboratory Report # UCRL-50349; 1967.
12. Wilkins M, et al. *Third progress report of the light armor program*. Lawrence Radiation Laboratory Report # UCRL-50460; 1968.
13. Wilkins M, Cline C, Honodel C. *Fourth progress report of the light armor program*. Lawrence Radiation Laboratory Report #UCRL-50694; 1969.
14. Wilkins M, Landingham R, Honodel C. *Fifth progress report of the light armor program*. Lawrence Radiation Laboratory Report # UCRL-50980; 1971.
15. Wilkins M, Landingham R, Honodel C. *Light armor*. Lawrence Radiation Laboratory Report # UCRL-71817; 1969.
16. Woodward RL. A simple one dimensional approach to modeling ceramic composite armour defeat. *Int J Imp Eng* 1990;**9**(4):455–74.
17. LaSalvia JC. A physically-based model for the effect of microstructure and mechanical properties on ballistic performance. *Ceram Eng Sci Proc* 2002;**23**(3):213–20.
18. Krell A, Straßburger E. Hierarchy of key influences on the ballistic strength of opaque and transparent armor. *Adv Ceram Armor III: Ceram Eng Sci Proc* 2008;**28**(5):45–55.
19. Hauver GE, Netherwood PH, Benck RF, Rapacki EJ. Ballistic performance of ceramic targets. In: *Proceedings of the 13th Army Symposium on Solid Mechanics*. 1993.
20. Hauver GE, Netherwood PH, Benck RF, Kecskes LJ. Enhanced ballistic performance of ceramic targets. In: *Proceedings of the 19th Army Science Conference*. 1994.
21. Wilkins M. Mechanics of penetration and perforation. *Int J Eng Sci* 1978;**16**(11):793–807.
22. Kanel GI, Nellis WJ, Savinykh AS, Raorenov SV, Rajendran AM. Effect of crystalline anisotropy on shock propagation in sapphire. In: *AIP Conf Proc, 1195*. 2009. p. 851–4.
23. Kanel GI, Nellis WJ, Savinykh AS, Raorenov SV, Rajendran AM. Response of seven crystallographic orientations of sapphire crystals to shock stresses of 16–86 GPa. *J Appl Phys* 2009;**106**(4).
24. Subhash G. Dynamic indentation testing. In: Kuhn H, Medlin D, editors. *ASM handbook on mechanical testing and evaluation*, vol. 8. Materials Park, OH: ASM International; 2000. p. 519–29.
25. Anton RJ, Subhash G. Dynamic Vickers indentation of brittle materials. *Wear* 2000;**239**:27–35.
26. Ghosh D, Subhash G, Sudharshan TS, Radhakrishnan R, Gao X. Dynamic indentation response of fine-grained boron carbide. *J Am Ceram Soc* 2007;**90**(6):1850–7.
27. Klecka M, Subhash G. Rate dependant indentation response of structural ceramics. *J Am Ceram Soc* 2010;**93**(10):2377–83.
28. Nowak R, Sekino T, Niihara K. Non-linear surface deformation of the (1 0 1 0) plane of sapphire: identification of the linear features around spherical impressions. *Acta Mater* 1999;**47**(17):4329–38.
29. Chaudhri MM, Wells JK, Stevens A. Dynamic hardness, deformation and fracture of simple ionic crystals at very high rates of strain. *Philos Mag A* 1981;**43**(3):643–64.
30. Wang S, Pirouz P. Mechanical properties of undoped GaAs. III. Indentation experiments. *Acta Mater* 2007;**55**:5526–37.
31. Jennett NM, Nunn J. High resolution measurement of dynamic (nano) indentation impact energy: a step towards the determination of indentation fracture resistance. *Philos Mag* 2010:21.
32. Tymiak NI, Daugela A, Wyrobek TJ, Warren OL. Acoustic emission monitoring of the earliest stages of contact-induced plasticity in sapphire. *Acta Mater* 2004;**52**:553–63.
33. Jones CD, Rioux JB, Locker JW, Bates HE, Zanella SA. Large-area sapphire for transparent armor. *Am Ceram Soc Bull* 2006;**85**(3):24–6.
34. Nemat-Nasser S, Isaacs JB, Starrett JE. Hopkinson techniques for dynamic recovery experiments. *Proc R Soc Lond A* 1999;**435**:371–91.
35. Lawn BR. *Fracture of brittle solids*. Cambridge: Cambridge University Press; 1995.
36. Meyer E. Untersuchungen über Härteprüfung und Härte. *Z Ver Dtsch Ing* 1908;**52**(17):645–54.
37. Li H, Bradt CR. The microhardness indentation load/size effect in rutile and cassiterite single crystals. *J Mater Sci* 1993;**2**(4):917–26.
38. Li H, Suematsu H, Iseki T, Bradt RC. Microhardness anisotropy and the indentation load/size effect in $MgO \cdot xAl_2O_3$ single crystals. *J Ceram Soc Jpn* 1991;**99**(11):1079–87.
39. Masaki K, Stevenson ME, Bradt RC. Knoop microhardness anisotropy and the indentation size effect on the basal plane of single-crystal alumina (sapphire). *J Am Ceram Soc* 2002;**85**(2):415–22.
40. Attinger C. Orientation and hardness of synthetic corundum. *Ind Diam Rev* 1952;**12**(1):136–7.
41. Hockey BJ. Plastic deformation of aluminum oxide by indentation and abrasion. *J Am Ceram Soc* 1971;**54**(5):223–31.
42. Kollenberg W. Plastic deformation of Al_2O_3 single crystals by indentation at temperatures up to 750 °C. *J Mater Sci* 1988;**23**:3321–5.
43. Chan HM, Lawn BR. Indentation deformation and fracture of sapphire. *J Am Ceram Soc* 1988;**71**(1):29–35.
44. Farber BY, Yoon SY, Lagerlöf KPD, Heuer AH. Microplasticity during high temperature indentation and the Peierls potential in sapphire (Al_2O_3) single crystals. *Phys Status Solidi A* 1993;**137**(2):485–98.
45. Cook RF, Pharr GM. Direct observation and analysis of indentation cracking in glasses and ceramics. *J Am Ceram Soc* 1990;**73**(4):787–817.
46. Nowak R, Sakai M. The anisotropy of surface deformation of sapphire: continuous indentation of triangular indenter. *Acta Metall Mater* 1994;**42**(8):2879–91.
47. Nowak R, Sekino T, Niihara K. Surface deformation of sapphire crystal. *Philos Mag A* 1996;**74**(1):171–94.
48. Nowak R, Sekino T, Maruno S, Niihara K. Deformation of sapphire induced by a spherical indention on the (1 0 1 0) plane. *Appl Phys Lett* 1996;**68**(8):1063–5.
49. Kim YG, Kim DK. In situ observation of fracture sequence of physical vapor deposited TiN film on (1 1 2 0) sapphire. *J Mater Res* 2005;**20**(6):1389–95.
50. Tymiak NI, Gerberich WW. Initial stages of contact induced plasticity in sapphire. I. Surface traces of slip and twinning. *Philos Mag* 2007;**87**(33):5143–68.
51. Tymiak N, Chrobak D, Gerberich W, Warren O, Nowak R. Role of competition between slip and twinning in nanoscale deformation of sapphire. *Phys Rev B* 2009;**79**:174116.
52. Haney EJ, Subhash G. Analysis of interacting cracks due to sequential indentations on sapphire. Acta Mater (2011), doi:10.1016/j.actamat.2011.02.026.